Tiseira, A.; García-Cuevas González, LM.; Quintero-Igeño, P.; Varela-Martínez, P. (2022). Series-hybridisation, distributed electric propulsion and boundary layer ingestion in long-endurance, small remotely piloted aircraft: Fuel consumption improvements. Aerospace Science and Technology. 120:1-11. https://doi.org/10.1016/j.ast.2021.107227

Series-hybridisation, distributed electric propulsion and boundary layer ingestion in long-endurance, small remotely piloted aircraft: fuel consumption improvements

Andrés Omar Tiseira Izaguirre[a], Luis Miguel García-Cuevas González[a,*], Pedro Quintero Igeño[a], Pau Varela Martínez[a]

[a] *CMT – Motores Térmicos. Universitat Politècnica de València.*

Abstract

Series hybridisation, distributed electric propulsion (DEP) and boundary layer ingestion (BLI) are some of the most promising approaches for fuel consumption reductions in general aviation and commercial air transport. While these technologies can be also adapted for long endurance and long range, propeller-driven, small remotely piloted aircraft, their beneficial effects are not so clear due to the relatively high increase in propulsion system weight and the reduction in efficiency of the lower Reynolds number propellers. Using weights and efficiencies of off-the-shelf components, this work studies the impact of series hybridisation with and without DEP and BLI in a long endurance, 25 kg of maximum takeoff mass fixed wing aircraft, showing promising results with fuel consumption reductions of more than 15 %.

Keywords: Unmanned Aerial Vehicle; Electric Propulsion; Airframe-Propulsion Integration; Hybrid System; Propeller; Boundary Layer Ingestion

1. Introduction

During the past years it has been observed an important increase on the use and commercialisation of Remotely Piloted Aircraft Systems (RPAS), and the data available in the literature suggest this trend will be maintained in the future. In fact, in accordance with a report published by the Single European Sky ATM Research [1], it is predicted that, during the next 15 years, the fleet of RPAS will reach hundreds of thousands of units. In the face of such an increase, it is necessary to research for more efficient aircraft models, optimising, among others, the powertrain and the aerodynamic design, as mentioned by NASA in the ITDs of the Environmentally Responsible Aviation (ERA) project [2]. This need has recently prompted the investigation of new unconventional configurations of small aircraft, as can be seen in the works of Zhang et al. [3], where the propulsion of a quadrotor fixed-wing hy-

*Corresponding author.
E-mail address: luiga12@mot.upv.es

brid unmanned aerial vehicle is optimised, and Rostami et al. [4], in which aerodynamic performance is improved in an UAV through the interaction and design of tandem ducted propellers.

Although electric propulsive powertrains are usually characterised by the low energy density of batteries in comparison with fuel-based powertrains, this is normally compensated in small low speed RPAS by their low maintenance cost and ease of control, as shown in [5]. Internal combustion engines (ICE) are relegated to bigger, faster or longer endurance aircraft. ICE may even be used in smaller RPAS where extreme thrust-to-weight ratios are needed, as in acrobatic aircraft, as a higher thrust may be more important than the big thermal losses of small ICEs [6, 7, 8]. The output torque of spark ignition ICEs is usually controlled by means of a throttle valve, as they burn in stoichiometric conditions, which leads to a high fuel consumption when working at partial loads. In order to overcome this, novel approaches are being developed. The engine output torque can also be controlled by burning lean, thus maintaining high efficiencies and maintaining the emissions of unburnt hydrocarbons, CO and NO_x at very low levels. There are important advancements being produced today in this area, ranging from understanding of the combustion process in lean combustion in engines with pre-chamber [9]

to advanced concepts such as water insulation to reduce heat transfer at very high compression ratios [10]. These engines come, however, with a weight penalty, which may limit their use to bigger RPAS.

An intermediate configuration is possible, where an ICE is used to drive an electrical generator that powers electric motors. This configuration, called electric hybridisation or hybrid-electric (HE), allows combining the benefits of both powertrains. As compared to the pure electric propulsion, its main advantage is the increase in endurance and range, as shown in [5], due to the use of fossil fuels, with higher energy densities. On the other hand, and assuming perfect combustion, HE allows reducing CO_2 emissions compared with pure combustion engines, by using non-conventional engine configurations such as distributed electric propulsion or DEP, because these configurations require less fuel to fly the same range. In the literature, Kim et al shows the benefits of combining both technologies in [11].

The incorporation of electrical hybridisation in RPAS has been widely studied in recent years, although it is true that most studies focus on parallel hybridisation. Among these works, it would be worth mentioning the research of Auesser et al. [12], where they integrate and validate a parallel HE propulsion system for RPAS; the work of Harmon et al. [13], who proposed

an optimisation on both aerodynamics and the HE propulsive system; or Kim et al. [14], who focused in the fuel economy optimisation of parallel HE. A parallel configuration allows connecting both the electric motor and ICE to the propeller shaft, which implies smaller engines that together achieve the necessary power. This flight mode reduces the acoustic footprint and is suitable for surveillance missions, as reviewed by Mengistu in [15]. However, a series configuration is also attractive. In series HE the ICE is operating at a fixed and optimal point driving a generator. The ICE is decoupled from the propeller shaft and the generator powers the electric motors [16].

Despite not allowing pure-electric flight, the operational independence between ICE and electric engines allows novel configurations such as DEP, which can improve the design of the aircraft. It also allows decoupling the rotational speed of the propeller from that of the internal combustion engine, which allows individual optimisation of the operating point of the ICE and the electric motor.

Due to its optimisation capabilities, DEP has been studied during past years both for conventional and small RPAS. In the research of Stoll et al. [17, 18], this configuration is tested proving multiple advantages as ease of maintenance and replacement of high-efficiency electric engines, increased

flow circulation on the wing increasing the aerodynamic efficiency, or the use of the propulsion system as a control platform, reducing the size and use of flaps and aerodynamic actuators. Further improvements can be seen in the research of Chen and Zhou [19, 20], where they demonstrate both computationally and experimentally that the lift-to-drag ratio can be increased through the successful design of a base propeller/wing integration.

For optimisation of a DEP system, the location of the engines have shown to have a not-negligible effect over the aerodynamic behaviour of the aircraft. If the distribution of small electric motors over the entire wingspan is made at the trailing edge, instead of using a traditional configuration or leading-edge distribution, it is possible to take advantage of the effect of the engine boundary layer ingestion, or BLI, as described in [21, 22, 23].

BLI is mainly based on flux re-acceleration on the airfoil due to boundary layer engine ingestion, which leads to a wake reduction and to less power needed by the engine. BLI increases the propulsive efficiency as the ingestion fraction grows, decreasing the power needed by the propeller for a given mass flow, as highlighted in [22, 24]. Likewise, the propeller ingestion modifies the airflow circulation above the wing, resulting in an increment of the suction peak at the leading edge of the wing reducing lift-induced drag, a

positive effect on aerodynamic efficiency that is weighed down by increased skin friction drag. However, considering the reduction of wake mixing losses due to suction and its associated drag, some authors such as Hall et al. [25] have found that the aerodynamic efficiency will be higher in BLI configurations. In the same way, Teperin et al., Martínez et al. and Samuelsson et al. [26, 27, 28] pointed out an improvement in aerodynamic efficiency due to a drag reduction when the BLI system is applied on fuselages.

Thanks to the combined use of DEP and BLI, it is possible to achieve a synergy between the propulsion system and the aerodynamics, or, in other words, a decrease in fuel consumption for the same flight range, as the DEP will allow the engines to ingest a greater amount of boundary layer formed on the wing. This phenomenon has been described by Goldberg et al. in [29].

Although the literature about hybrid electric propulsion, DEP or BLI in small fixed-wing aircraft shows promising results, there is limited information about using the three approaches at the same time in low speed, long range, small RPAS. The aim of the current research paper is to analyse the feasibility of implementing an aircraft configuration of series hybrid with a DEP plant and BLI. The research focuses on reducing the fuel consumption

of high range RPAS and, therefore, reducing the greenhouse gas emissions associated with RPAS with classic engines. The study is performed by means of computational tools, validated against experimental data whenever possible. The document is organised as follows. First, in section 2, a reciprocating ICE-powered, propeller-driven and long range small RPAS configuration is selected, including its engine and propeller. Then, in section 3, the main methods and models are presented. Finally, in section 4 the different results are computed for the best RPAS configuration, and compared with classical configurations, summarising those results in the conclusions in section 5.

2. Case description

In this section, the different design parameters and components are selected in order to set a large number of parameters before the optimisation.

One of the main design limitations is the aircraft's maximum takeoff mass ($MTOM$), which is fixed at 25 kg at most. This limitation is chosen considering the Spanish regulation for RPAS civil use [30], as well as other similar regulations across Europe. The different aircraft geometric dimensions are based on a Penguin C from UAV Factory [31], being an aircraft of similar $MTOM$, with an ICE based powertrain. An RPAS of such characteristics

will have an endurance of more than 20 h, a flight speed between 20 m s^{-1} to 30 m s^{-1} and a power requirement of around 1 kW. The aircraft is tested in three different configurations: pure ICE propulsion, hybrid electric propulsion and hybrid with DEP and BLI.

The Honda GX-35 engine has been selected as ICE both for the baseline case and for the different hybrid cases. This engine has a maximum power of 1 kW at sea level, which complies with the maximum power required for the *MTOM* set in this study. Its brake specific fuel consumption ($BSFC$) map has been measured by Mengistu in [15] between 0 % and 60 % of its maximum torque: the author found instability issues during the measurement at higher torques. Maximum torque data can be found in other sources such as in [32]. Other researchers have previously used the engine, as it has been found in studies for aircraft of similar weight mainly due to its high specific power, as shown in [12, 13, 33]. The baseline configuration has a propeller with a radius of 114.3 mm and a propeller gearbox with a fix speed ratio of 2.75. The speed ratio produced by the gearbox, which is the rotational speed of the propeller divided by that of the ICE, allows the former to rotate faster than the engine shaft, so that both the ICE and the propeller work optimally. The mechanical efficiency of the gearbox, η_m, is set as 0.9, an average value

for low ratio off-the-shelf products.

A single airfoil, the SD7003, is used for the entire wing due to its low parasitic drag at low and medium Reynolds numbers, $Re = \rho \cdot U \cdot c/\mu$, where ρ, U and μ are, respectively, the density, the velocity and the viscosity of the air, and c is the airfoil chord. Several research documents with experimental and computational data of this airfoil can be found in the literature to validate the simulations performed with it: [34, 35, 36, 37].

The chord length is set at 200 mm and constant in the complete wingspan b. An aspect ratio $\text{Æ} = b/c$ equal to 10 is assumed. All geometric data are summarised in Table 1. Some relevant aerodynamic parameters are also included: the parasitic drag coefficient due to the fuselage, empennage and other elements, not including the wing, $C_{D,0,\text{extra}}$; also, the Oswald efficiency factor, e. The total drag D is computed using these parameters as in Equation 1:

$$D = \frac{1}{2} \cdot \rho \cdot U^2 \cdot S \cdot \left(C_{D,0,\text{wing}} + C_{D,0,\text{extra}} + \frac{C_L^2}{\pi \cdot \text{Æ} \cdot e} \right) \tag{1}$$

where ρ is the far field air density, U is the upstream wind speed, S is the wing surface, $C_{D,0,\text{wing}}$ is the parasitic drag coefficient of the wing and C_L

is the lift coefficient. The values of $C_{D,0,\text{wing}}$ and $C_{D,0,\text{extra}}$ are computed using geometrical information of an aircraft with a similar mission, including the Penguin C in [31] and the Harmon and Hiserote's aircraft [12, 13]. The Oswald efficiency factor e has been calculated using also the information of similar aircraft and different methods described in [38] and [39]. Finally using the method proposed by Kroo, a value for e of 0.8 is set.

Table 1: Aerodynamic, design parameters and engine data

Design parameters	
Aspect ratio	10
Wing area	$0.4\,\text{m}^2$
Wing span	$2\,\text{m}$
Wing chord	$0.2\,\text{m}$
Maximum takeoff mass	$25\,\text{kg}$
Aerodynamic parameters	
$C_{D,0,\text{extra}}$ (fuselage, empennage, others)	0.011
Oswald efficiency factor (e)	0.8
Engine data	
Net power (at 7000 rpm)	$1\,\text{kW}$
Max. net torque (at 5500 rpm)	$1.6\,\text{N m}$
Dry mass	$3.33\,\text{kg}$

Due to the large impact of a correctly defined propeller on the problem, extensive geometry data is required. The DA4052 two-blade propeller designed by UIUC [40] is selected, for which the complete blade geometry and wind tunnel testing data are provided.

Additionally, in hybrid cases, an increase in operating empty mass due to the electrical parts will be assumed, establishing that the final mass will be approximately 5 % higher than the baseline case for DEP and BLI configuration and 3 % for the pure hybrid case. These masses have been estimated from typical off-the-shelf components, collected on Table 2, counting the added mass of propellers, electric motors, an electric generator and electronic speed controllers (ESC). The mass increase estimated from off-the-shelf components is consistent with what is calculated in the literature, as can be seen in Harmon's research [13].

The selected elements obey the design, weight and power required of an aircraft of the characteristics described so far. However, they are not in any case the final design elements of this aircraft. Their selection has the sole objective of correctly estimating the differences in weight between the different types of RPAS described.

The operating empty mass penalty of the DEP plus BLI configuration can be mitigated due to the distribution of the weight of the propulsive system over the wing: the bending moment in the wing root is decreased due to this, so a decrease in its structural weight can be expected in an aircraft designed for operating with DEP. However, this potential reduction in the operating

empty mass has not been taken into account in this study.

Table 2: Off-the-shelf components. masses and prices

HE + DEP + BLI			
Element	**Name**	**Mass [kg]**	**Price [€]**
Generator	Turnigy Aerodrive SK3 - 4250-410kv	0.260	41.35
Motor	Turnigy 4500kv 2610 EDF Outrunner	0.054	11.39
ESC	Turnigy Multistar 32 bits 12 A Race Spec ESC	0.006	5.23
Rectifier	3 Phase Rectifier Bridge Powersem PSD 82	0.160	50.92
Wire	AWG 22 and AWG12	0.100	47.95
Propeller	APC 4.1x4.1E	0.003	5.46
	Total extra increase for 13 propellers	1.351	427.26
	Increase relative to baseline case [%]	5.40	
HE single engine			
Element	**Name**	**Mass [kg]**	**Price [€]**
Generator	9225-160KV Turnigy Multistar	0.329	92.84
Motor	NTM Prop Serie Drive 35-36A 1800KV/875W	0.126	25.06
ESC	YEP 80A SBEC	0.070	43.99
Rectifier	3 Phase Rectifier Bridge Powersem PSD82	0.160	50.92
Wire	AWG 12	0.018	47.95
Propeller	APC B9x9E	0.018	8.43
	Total extra increase	0.721	260.76
	Increase relative to baseline case [%]	2.9	

Table 2 also shows the indicative retail price (subject to change) of the additional components that include both hybrid configurations. The price of the HE DEP BLI configuration is higher since several extra components are carried. This initial outlay could be mitigated thanks to the savings in the

fuel consumption of this configuration.

A sketch of the aircraft can be seen in Figure 1 to aid in its visualization. This sketch is not to scale nor does it obey the final design in any case.

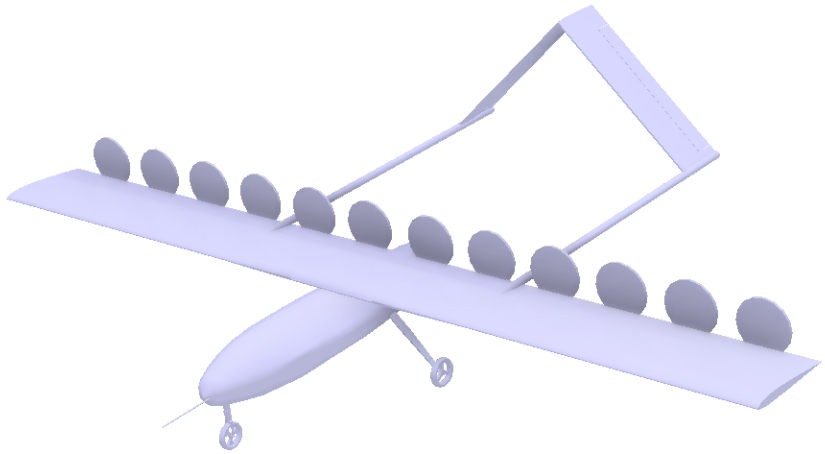

Figure 1: Preliminary sketch of the full RPAS with HE DEP BLI, not to scale

3. Methodology

In this section, the different computational models used in order to calculate the performance of different RPAS configurations are presented. First the computational domain is presented. Then, the computational fluid dynamics (CFD) method used to compute the series hybridisation with DEP

and BLI is explained. CFD simulations are performed with different configurations: a section of the wing, a single propeller and a section of the wing with a propeller in the trailing edge. These simulations serve as input to a model to compute the range of the aircraft in different conditions.

3.1. Computational setup

The case studies are composed of a large domain, a wing section and an actuator disc that simulates the propeller.

This domain can be observed with its main dimensions and the mesh in Figure 2.

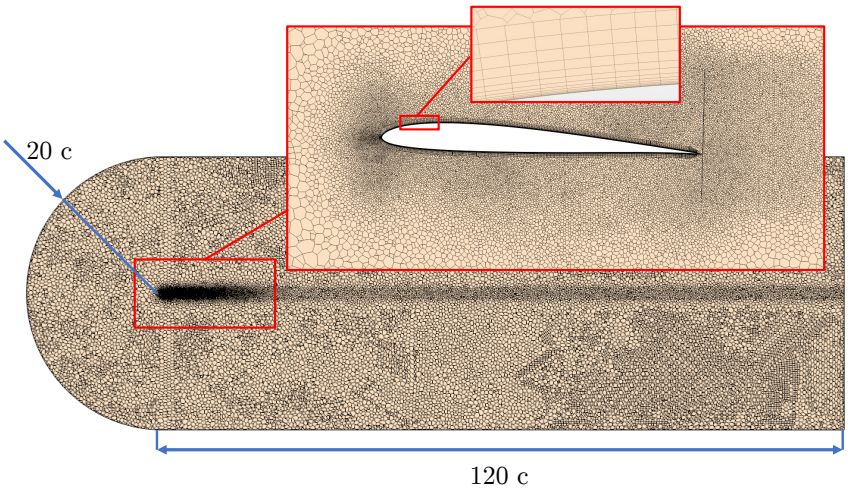

Figure 2: Sketch of the computational grid used for the current calculations

Regarding the boundaries, the upwind boundary condition is set 20 chords

away from the wing, imposing the free-stream speed on it by means of a velocity inlet boundary with constant speed, as well as the turbulence intensity and length scale by means of a turbulent viscosity ratio. The turbulent viscosity ratio is set to 0. This way, the turbulent intensity is equally 0, simulating a flight with negligible turbulence. The boundary downstream of the wing is set as a pressure outlet located 120 chords away from the wing. The boundary around the wing is set as a wall with smooth, no-slip conditions. Lateral boundaries are set as symmetry conditions, and the rest of the boundaries, located far from the body are modelled assuming that normal derivatives of the variables are zero at these locations. The boundaries above and below the wing are separated from it by 40 chords in order to ensure that their location do not unphysically affect the results. This domain size is common, as can be seen in other research on CFD aerodynamics [41].

To verify that the dimensions of the domain are sufficient and do not interfere with the solution, a domain independence analysis was performed. For this, two additional cases were carried out, one with a domain with half the vertical height (20 chords) and the other doubling said height (80 chords). All cases have the same mesh base size and have been carried out using a Reynolds number of 5×10^5 and an angle of attack of $3°$. The mesh base size

in all the simulation cases is defined as the size of the mesh over the airfoil surface. The results of the independence study can be seen in Table 3.

Table 3: Domain independence study

Domain height	C_L [-]	C_L **variation** [%]	$C_{D,0,\text{wing}}$ [-]	$C_{D,0,\text{wing}}$ **variation** [%]
$20c$	0.484 96	0.24	0.007 35	2.23
$40c$	0.486 12		0.007 19	
$80c$	0.487 16	0.21	0.007 12	0.97

The difference in drag coefficient between the selected domain height and a domain twice as large is 1 %, being this difference smaller for the lift coefficient. The effects in the solution due to the proximity of the far field boundaries is small enough to be considered negligible.

In the modelling of the wing with DEP and BLI, all simulations consist of a three-dimensional section of the wing with a virtual disk near the trailing edge, which simulates the propeller by means of the Blade Element Momentum Theory (BEMT), which will be explained later. The airfoil and the propeller are sketched in Figure 3.

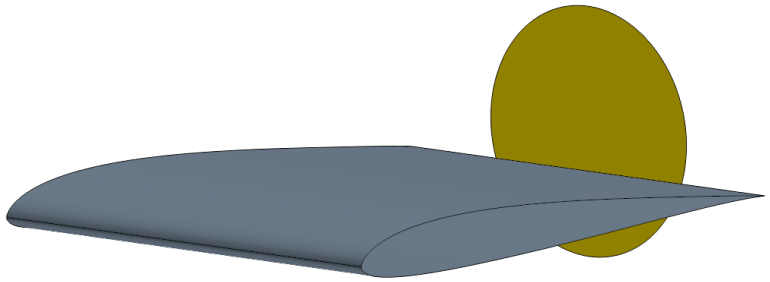

(a) Section of wing simulated with virtual disk

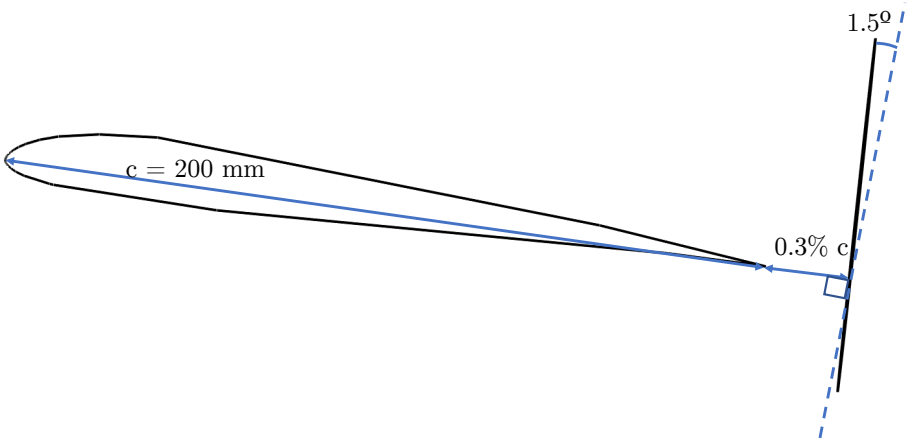

(b) Side-view with principal heights (not to scale)

Figure 3: DEP BLI case sketch used in CFD

Different propeller radius r are calculated between 30 mm, and 50 mm, with different distributions of propellers across the wingspan ranging between 12 and 25. This distribution is simulated by changing the domain width, supposing that the majority of the wing is sufficiently far from the wingtips.

These 2.5D simulations are configured to consider different propeller distributions. Maintaining the propeller radius and total wingspan, by changing the domain width and assuming that all propellers are equally spaced, the total number of propellers can be selected. A lower number of propellers translates into a faster propeller rotational speed to maintain the required thrust. Changes in the rotational speed while maintaining the same flow speed results in a displacement of the propeller operating point and a different propulsive efficiency. Also, fewer propellers mean a smaller portion of the wing influenced by the effect of the BLI, producing variations in the aerodynamic efficiency.

For each of these radii, different vertical positions are used in the calculation. This position is given by the relative distance between the trailing edge and the centre of the propeller. The lower position corresponds to 0 %, where the propeller is centred in the trailing edge, and the higher position to 100 %, where the propeller is completely upon the trailing edge. In Figure 4

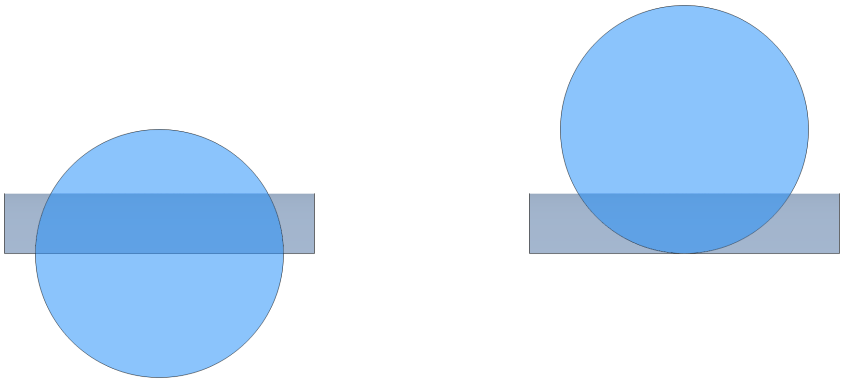

(a) 0 % position (b) 100 % position

Figure 4: Maximum and minimum propeller position above the trailing edge

the different positions are shown, looking at the wing from the trailing edge.

Besides from changing the propeller size, the number of propellers and their vertical position, the draft angle, which is the angle formed between the propeller shaft and the airfoil chord, is also changed between 0° and 3°.

A constant length gap is set between the SD7003 airfoil body and the virtual disk equal to 0.3 % of the chord. As explained in [42], as the airfoil wake moves downstream, the wake dissipates due to viscous shear stress and more power is needed to move the propeller that ingests the wake. In order to increase the propulsive efficiency, ingestion must take place before the dissipation of the wake, so it is advisable to use a small gap length.

The modelling in the cases without DEP is different due to the lack of interaction between the propeller and the wing. Here, the wing and the propeller are studied separately, with the same parameters as the DEP BLI cases. By having a single propeller, its radius is fixed as constant at 114.3 mm.

3.2. CFD models

The CFD simulations are carried out using the commercial software Simcenter STAR-CCM+ with a finite-volume, steady-state, Reynolds-Averaged Navier-Stokes (RANS) equations approach.

All calculations were performed on a multiuser cluster, using 8 Intel Xeon Gold 6154 CPUs per case, and simulation times are estimated as 128 cpu-hours per case simulated.

The RANS equations are computed in every simulation in the same way as Torregrosa et. al. explains in [43]. In this case, a Spalart-Allmaras model is used to solve the turbulent viscosity transport equation. This turbulence model has been successfully used previously in research related to DEP and BLI [18, 44].

The air surrounding the wing is modelled as incompressible, as the Mach number was kept below 0.2 in all the simulated cases. This hypothesis is common in small propeller simulations, as in [45].

A second-order linear upwind scheme is used to reconstruct the solution for the advection terms. A second order method is also used for the diffusive terms. The advection is computed by means of a Roe Finite Difference Splitting (FDS) method [46]. The gradients are computed with a hybrid Gauss-Least Squares Method with the Venkatakrishnan limiter [47]. The preconditioned coupled equations were solved with an implicit pseudo-temporal integration, with a variable and controlled Courant number, to keep the residuals limited. This method, although computationally more expensive than a segregated approach, proved to be more stable and to converge faster during the simulations with the propeller.

For discretisation, a polyhedral mesh is used. The polyhedral mesh is used in all the domain except in the boundary layer, where a prismatic mesh with a geometric grow distribution is applied with 14 layers and a total thickness of 3 mm, ensuring a y^+ lower than one in 99 % of the wall.

The mesh is sketched in Figure 2, where it is possible to observe the different refinement regions, as well as the detail near the wall and the prismatic layer.

A mesh independence analysis has also been carried out using a Reynolds number of 5×10^5 and an angle of attack of 3°. A generalised Richardson

extrapolation [48] is performed to estimate the value of the lift coefficient as a function of the mesh base size. Using several mesh sizes, the value of C_L for an infinitesimal base size is extrapolated as in Equation 2, where C is a constant, BS is the mesh base size and p is the global order of convergence.

$$C_L|_{BS} = \lim_{BS \to 0} C_L + C \cdot BS^p \tag{2}$$

C_L data for the finest meshes is summarised in Figure 5, highlighting the selected mesh size.

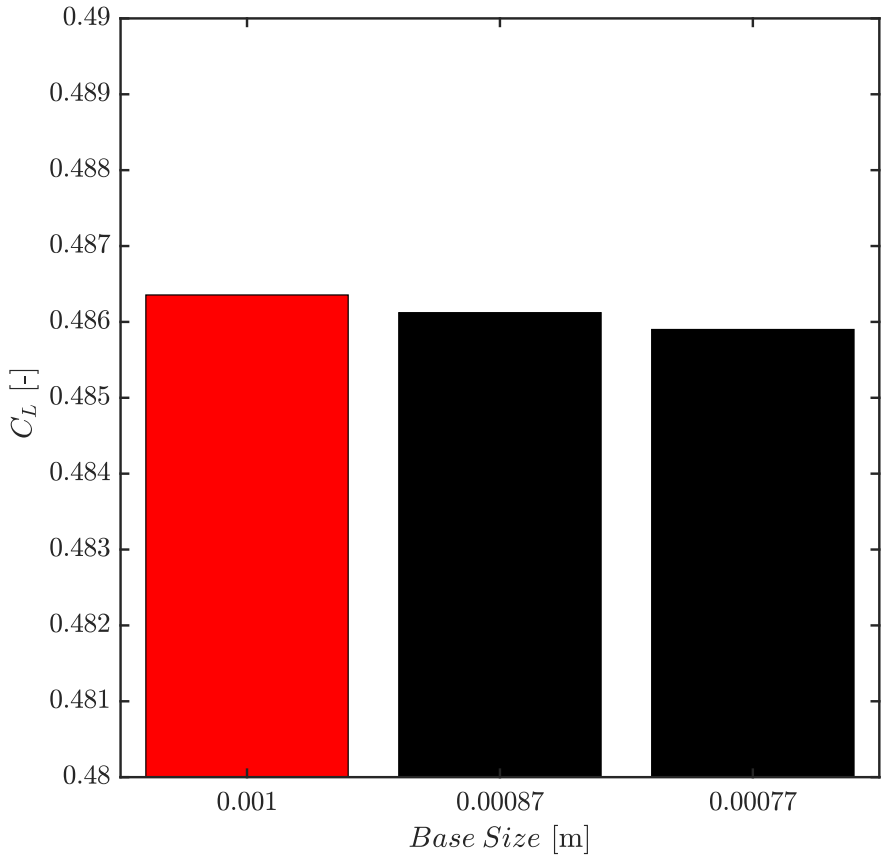

Figure 5: C_L data for each mesh with selected mesh highlighted

A mesh with a base size of 1 mm is set. The mesh convergence index, defined in [49], can be estimated as lower than 1 % using the 1 mm mesh, which is the one that will be used in all simulations. This convergence index provides an estimate of the amount of discretisation error in the selected grid

solution relative to the converged numerical solution.

The 2D airfoil polar has been validated against experimental data described in section 2. The validation can be seen in figure 6.

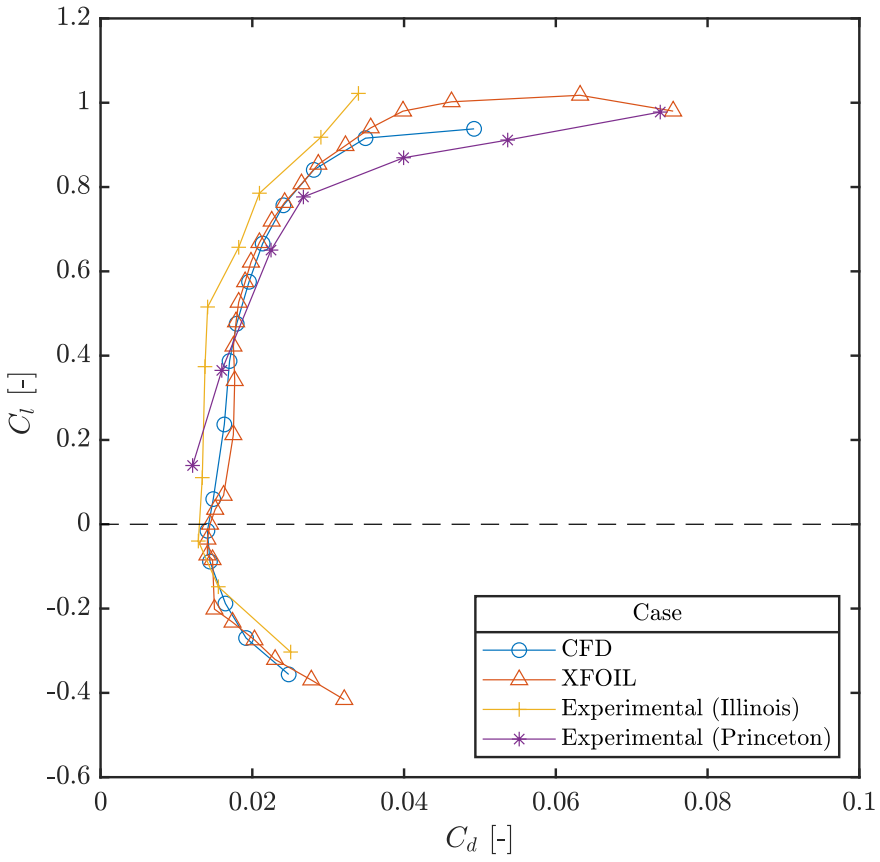

Figure 6: 2D CFD Polar validation with XFOIL data and experimental data measured by Selig in University of Illinois in Urbana Champaign (1995) and Princeton University (1989).

The results coincide with what has been experimentally measured by other authors. Although there are some differences between the results from UIUC and Princeton, they are attributed to some changes in model rugosity and manufacturing tolerances.

3.2.1. Actuator disk setup

The propeller is modelled using an actuator disk, or virtual disk, approach, coupled with a BEMT submodel. The virtual disk approach can be found in the literature for BLI and DEP analysis in [26, 18]. In the blade-element theory, the propeller blade is divided in different sections, where each element is characterised as a two dimensional wing. The total number of sections is set through a resolution parameter, which must be chosen according to the size of the mesh around the actuator disc.

The blade tip has a three dimensional aerodynamic behaviour, so a tip loss correction factor is fixed as constant and equal to 0 at a relative span of 0.97, as advised in [50]. The geometry of the blade was chosen to be the same as [40]. The aerodynamic coefficients for the BEMT method are calculated using XFLR5 [51], which uses XFOIL [52] to compute a solution of the airfoil using a potential flow method with interactive boundary layer corrections.

The propellers were also simulated without the wing and their results were

compared against experimental data, as shown in Figure 7. In this figure, the propulsive efficiency $\eta_p = (T \cdot U)/P$, where T and P are the propeller thrust and power respectively, is compared in a wide range of advance ratio $J = U/(n \cdot d)$, where n is the propeller rotational speed and d its diameter. Fair agreement was found between BEMT and experimental results.

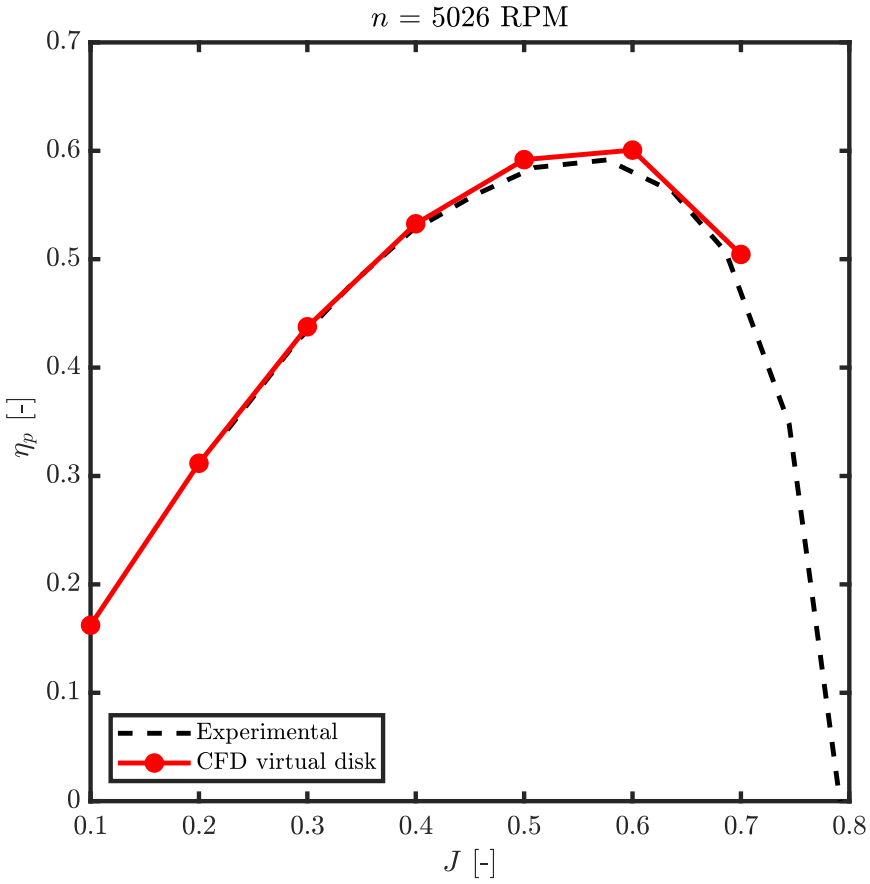

Figure 7: CFD and experimental propulsive efficiency comparison at 5026 rpm. Experimental data provided by [36]

The same modelling approach is used when computing the DEP and BLI cases. Since a single propeller is simulated, its rotational speed must be chosen for the BEMT in such a way as to take into account the thrust that

all propellers would produce. To this effect, the rotational speed is set so the thrust produced by all of them is equal to the total drag of the aircraft during each simulation. This hypothesis assumes that all propellers generate the same amount of thrust, since the flight is stationary and levelled.

The total aircraft drag is estimated from the simulation force coefficients and an extra $C_{D,0}$, which takes into account the rest of the drag that is not produced by the wing, as explained in section 2. This way, the total thrust of the aircraft, $T \cdot n_{\text{propellers}}$, is set equal to the total drag, D, as in Equation 3:

$$T \cdot n_{\text{propellers}} = D \tag{3}$$

where the propeller thrust, T, is multiplied by the total number of propellers, $n_{\text{propellers}}$. The total drag D is defined in Equation 1.

3.3. Range estimation

After obtaining the performance parameters of the wing, propeller, and wing plus propellers in DEP plus BLI configurations, these data were used to compute the range of the aircraft. First, the optimal range of the baseline configuration was computed.

The baseline configuration was selected in order to maximise the range

of the aircraft for a typical surveillance mission at low altitude, neglecting the time expended during take-off and landing and using a fuel mass m_{fuel} equal to 10 kg. The range of the baseline configuration, R_{baseline}, is computed numerically integrating Equation 4 between the initial mass $m_{\text{landing}}+m_{\text{fuel}}$ of 25 kg and the landing mass m_{landing} of 15 kg, taking into account the changes in the mass m and flight speed in the propulsive efficiency η_p, the aerodynamic efficiency C_L/C_D and the brake specific fuel consumption *BSFC*. A standard gravity of $9.806\,65\,\text{m}\,\text{s}^{-2}$ is used as the value for the acceleration due to gravity g.

$$R_{\text{baseline}} = \int_{m_{\text{landing}}}^{m_{\text{landing}}+m_{\text{fuel}}} \frac{\eta_p \cdot \eta_m}{BSFC \cdot g} \cdot \frac{C_L}{C_D} \cdot \frac{\mathrm{d}m}{m} \tag{4}$$

The flight speed U changed parametrically with the aircraft mass, following Equation 5, where U_0 is the speed for 0 mass and λ is the slope of the flight speed law.

$$U = U_0 + \lambda \cdot m \tag{5}$$

Both U_0 and λ were selected in order to maximise the range of the aircraft. The speed evolution during the mission progress is shown in Figure 8, where

the velocity law maintains a high specific range β, which is the integrand in Equation 4, as the mass decreases due to the fuel consumed. β is defined as in Equation 6.

$$\beta = \frac{\eta_p \cdot \eta_m}{BSFC \cdot g} \cdot \frac{C_L}{C_D} \cdot \frac{1}{m} \tag{6}$$

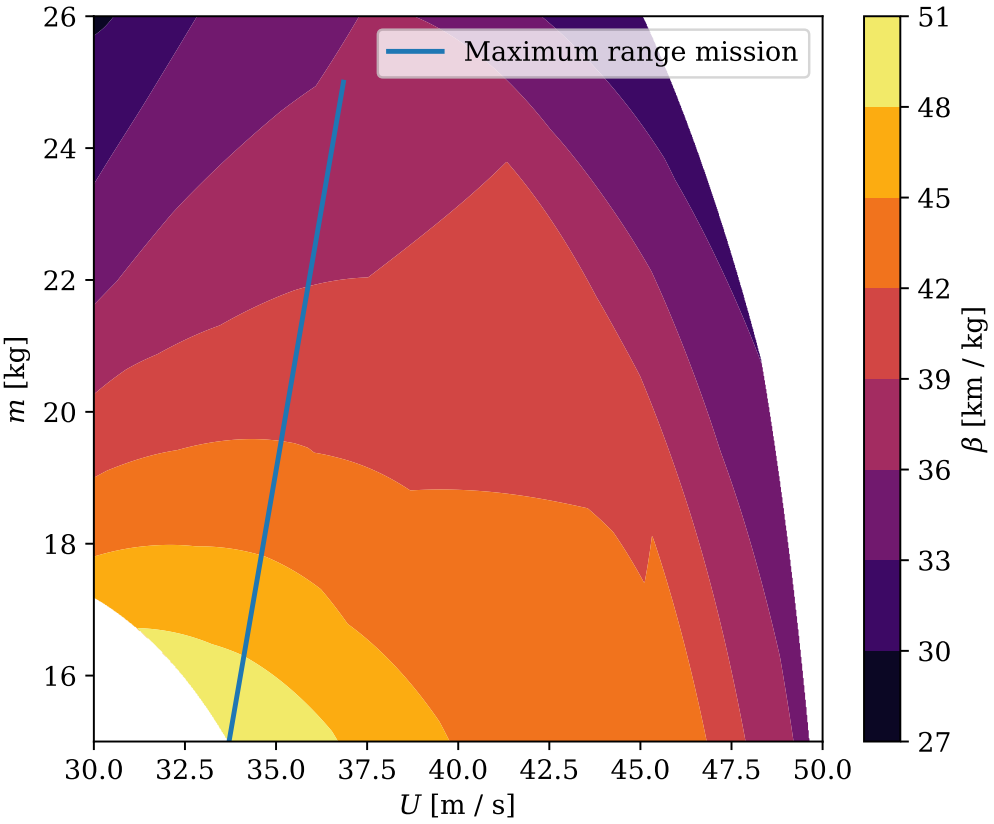

Figure 8: Baseline case velocity law which maximises the specific range

To obtain the velocity law that maximises the range both in the baseline

case and in the hybrids, the Broyden-Fletcher-Goldfarb-Shanno (BFGS) [53] algorithm is used, adding constraints to prevent the operation from performing in a lacking data area in the *BSFC* map.

The fuel used by the hybrid configurations is computed so their range is equal to that of the baseline case by solving Equation 7:

$$R_{\text{hybrid}} = R_{\text{baseline}} = \int_{m_{\text{landing,hybrid}}}^{m_{\text{landing,hybrid}}+m_{\text{fuel}}} \frac{\eta_p \cdot \eta_e}{BSFC \cdot g} \cdot \frac{C_L}{C_D} \cdot \frac{\mathrm{d}m}{m} \tag{7}$$

where $m_{\text{landing,hybrid}}$ is the operating empty mass plus payload of the hybrid configuration and η_e is the efficiency of the conversion of the mechanical power of the internal combustion engine to electrical power, the distribution of that electrical power to the electrical motors and the conversion back to mechanical power for driving the propellers. This efficiency, η_e, is set to a typical value of 0.8.

In series hybrid cases, because the propeller is not coupled with the ICE, the flight speed is chosen in such a way that it optimises the specific range during flight at every moment, resulting in a non-linear evolution of the velocity during flight. In Figure 9 it is observed that the speed that minimises the fuel consumption is higher than that of the baseline case. The minimum mass in this case, which is equal to the operating empty mass plus

the payload, is higher than in the baseline case due to the extra components needed.

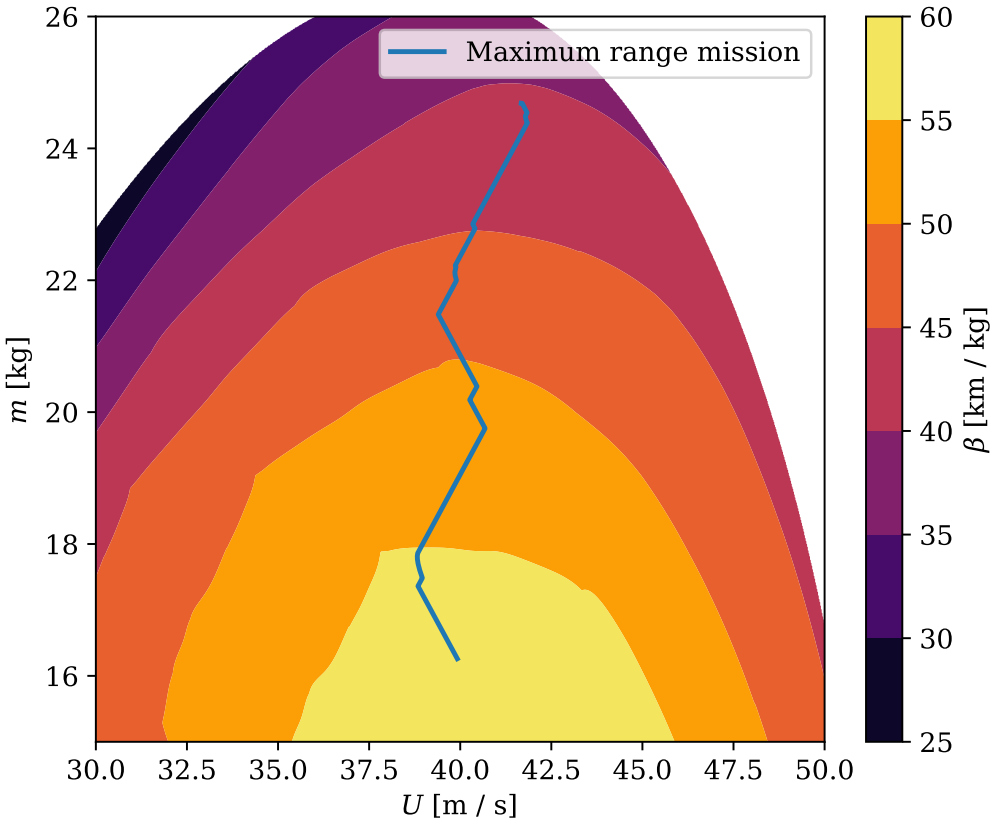

Figure 9: HE DEP BLI case velocity law which maximises the specific range

On each point, the aerodynamic and propulsive efficiencies are interpolated from data produced with CFD simulations. Meanwhile the operating point of the internal combustion engine and, hence, its *BSFC*, is set so its power output is equal to the power consumption by all the propellers and all the conversion losses, while minimising the fuel consumption.

In the hybrid cases, it is possible to optimise the $BSFC$ as a consequence of the decoupling between ICE and electric engines, since, for the necessary power, there will be no imposition of a rotational speed in the ICE.

In all cases, the rotational speed of the propellers was kept lower than the typical maximum speed for thin propellers for electric propulsion, as described in [54].

The results presented in section 4 are produced with the configuration with the lowest fuel consumption.

4. Results

As a result of the optimisation, a case with a propeller radius of 40 mm, a distribution of 13 engines on the wing and a draft angle of 1.5° with respect to the airfoil chord is selected.

The position above the trailing edge is fixed at 31.5 %. This result is based on a previous study carried out in [55], where the vertical position of the actuator disc is varied with respect to the trailing edge. In this study it is determined that the position described maximises the product of aerodynamic efficiency and propulsive efficiency.

The optimal DEP and BLI case is compared with the baseline case with-

out hybridisation and the pure hybridisation case without DEP. To this effect, the maximum range of the aircraft is calculated, obtaining a total of 4130 km. This operation is translated into the ICE map in Figure 10, where the *BSFC* is minimised taking into account the rotational speed necessary to maintain straight-and-level flight, since the engine in this case is mechanically coupled through the gearbox to the propeller. There are also extra constraints, ensuring that the engine always operates within its stable region.

Then, the operation of the hybrid cases is optimised for that range. Since in all hybrid cases the ICE is mechanically decoupled from the propeller shaft, the operation on the map behaves similarly: the ICE rotational speed is minimised to operate almost constantly at the lowest possible *BSFC*. The results are plotted over the same ICE map in Figure 10. The hybrid configurations tend to operate at low engine speeds and high torques, where the minimum *BSFC* values are obtained for this engine.

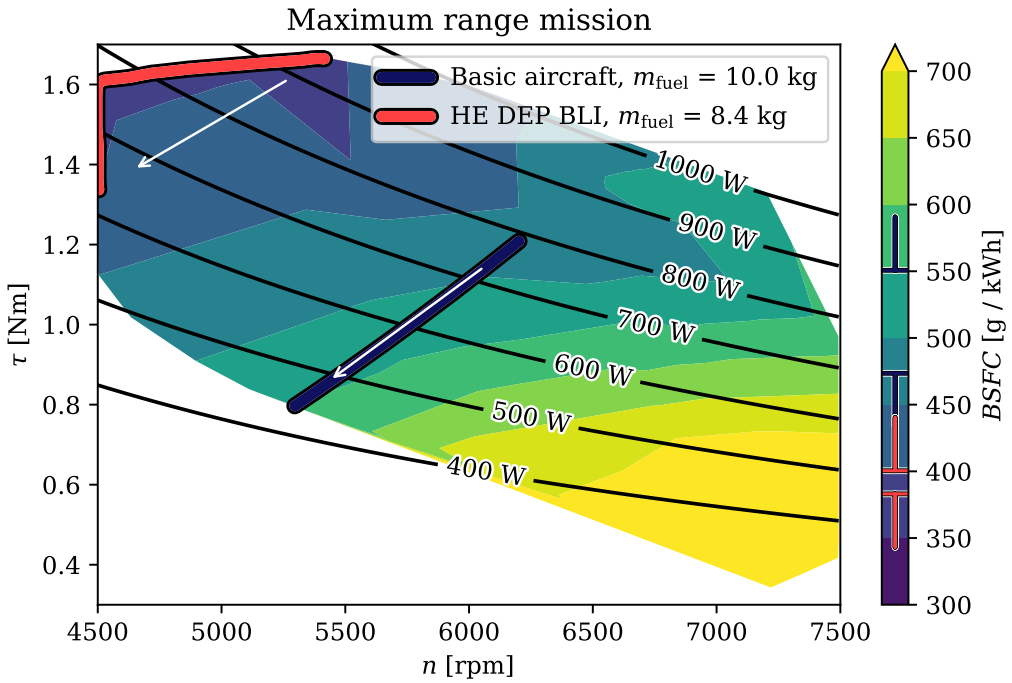

Figure 10: Maximum range mission evolution over the ICE map for the baseline case and the best HE with DEP and BLI case. White arrows indicate the direction of the ICE operation through the flight.

In Figure 10, white arrows indicate the direction of the ICE operation through the flight. This graphic includes in the colourbar the operational *BSFC* range of each case, and the final fuel mass used for the same range mission.

Figure 11 represents the velocity of each case as the mission progresses and the weight of the aircraft decreases. In the baseline case, as the flight progresses and fuel is consumed, the required power decreases. Aircraft ve-

locity also decreases progressively to ensure the lowest possible fuel consumption while meeting the required propeller rotational speed. The velocity law works differently in the hybrid cases because the propeller shaft is decoupled from the ICE: as the weight decreases, the speed increases and decreases to maintain an optimum and nearly constant specific fuel consumption, thus cushioning the drop in power.

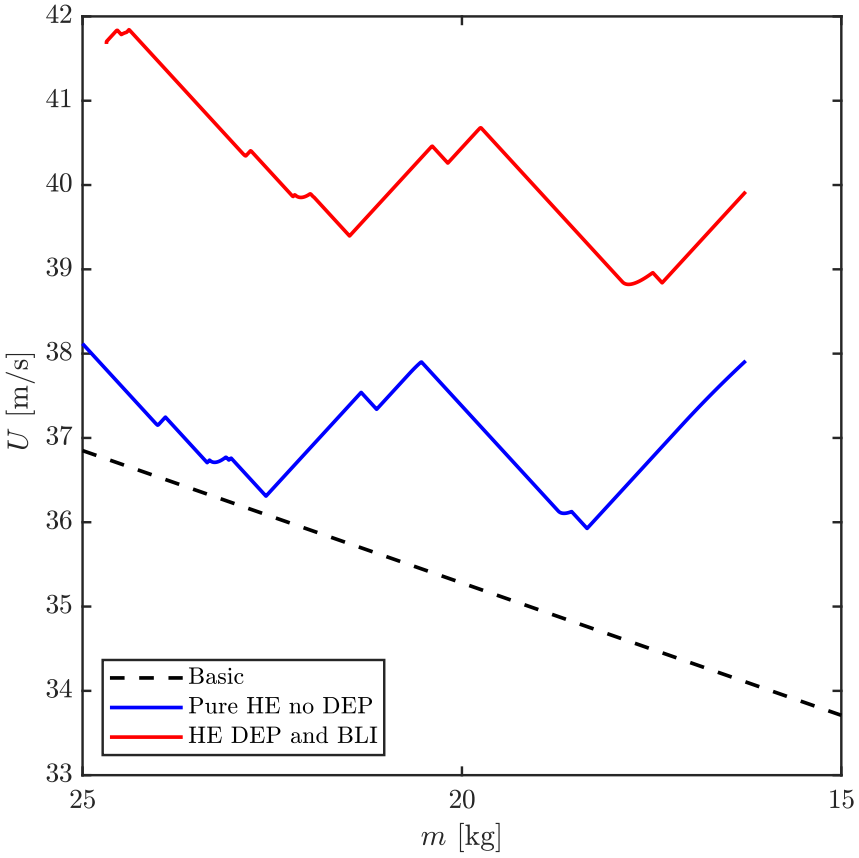

Figure 11: Aircraft speed comparison through the flight

The velocity law has a direct impact on the aerodynamic efficiency throughout the flight, where the high speeds in a large part of the flight make this efficiency drop rapidly, as can be seen in Figure 12. However, if both hybrid cases are compared, even if both have similar velocity behaviours, the hybrid

cases with DEP and BLI have a higher aerodynamic efficiency than the case without it.

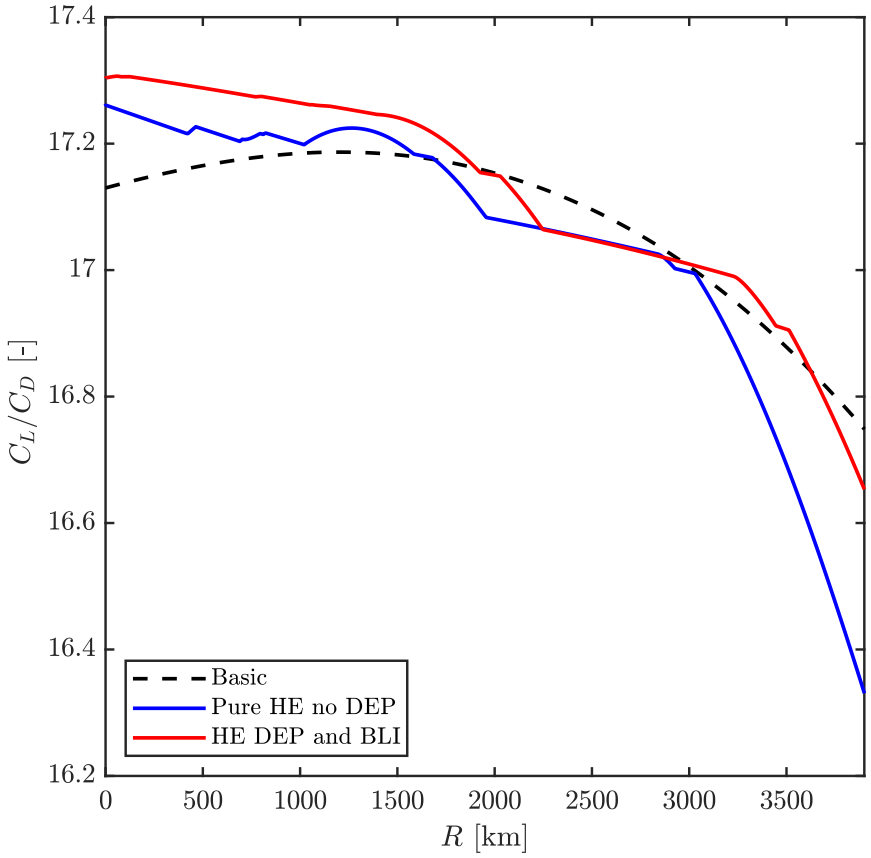

Figure 12: Aerodynamic efficiency comparison through the flight

The propulsive efficiency is represented in Figure 13. It can be seen that in the cases with a single propeller, both the baseline and the hybrid, work in

the zone of maximum propulsive efficiency, where both curves are superimposed on that of the simulated DA4052 propeller. Nonetheless, the propulsive efficiency of the case with DEP is superior. The effect of BLI increases this efficiency outside the baseline curve and it shifts the new curve towards a higher advance ratio. This way, the smaller propellers work in a zone of maximum propulsive efficiency 2.5 % higher than the baseline configuration.

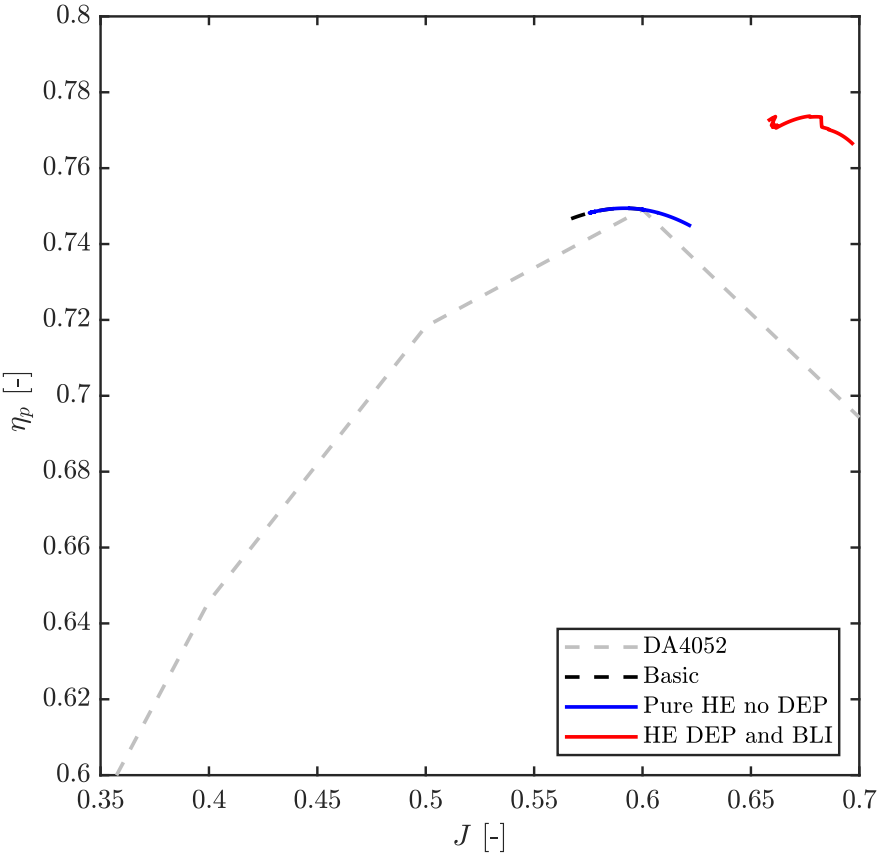

Figure 13: Propulsive efficiency through the flight

Both the CO_2 emissions throughout the flight, and the product of aerodynamic efficiency times propulsive efficiency divided by the *BSFC*, are represented in Figure 14 and Figure 15.

For the estimation of CO_2, a complete, stoichiometric and perfect com-

bustion is considered in any case, so that for every kg of fuel burnt 3.05 kg of CO_2 are obtained.

The efficiency product, which is the specific range times the mass of the aircraft, is a figure of merit that is relatively independent of the actual weight. This product will be referred as global efficiency in the rest of the document.

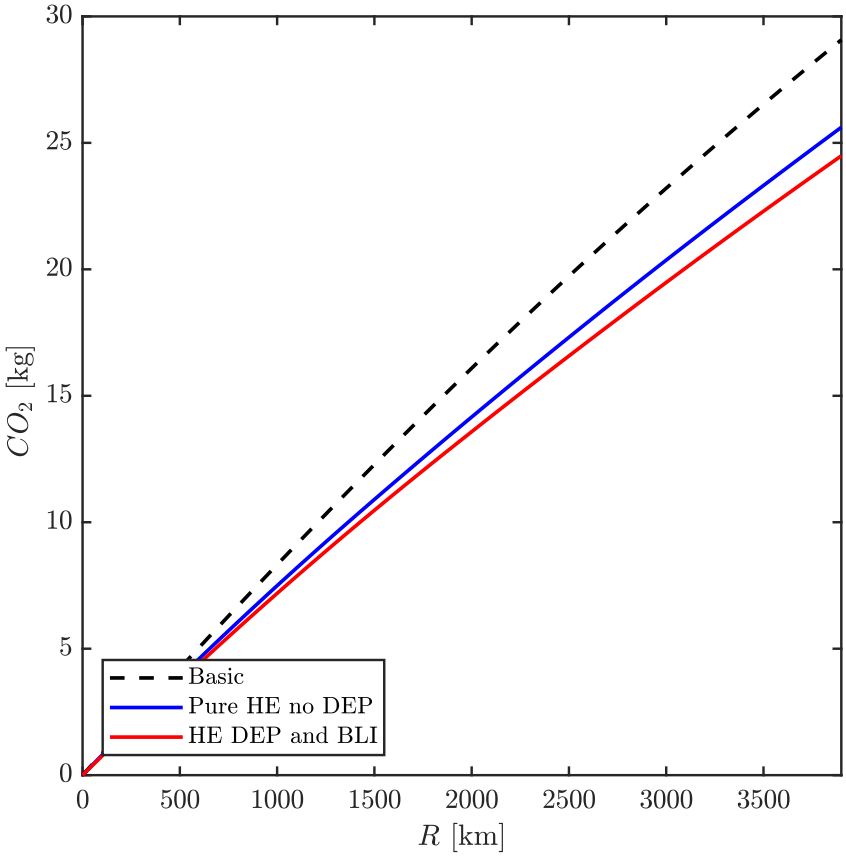

Figure 14: Aircraft CO_2 emission through the flight

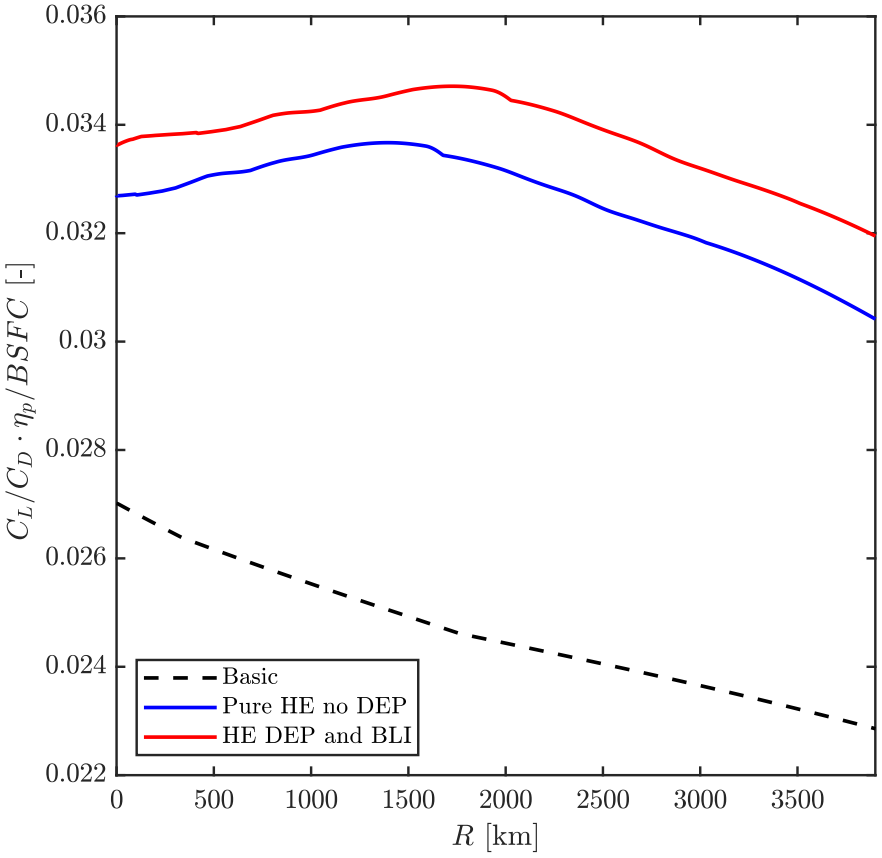

Figure 15: Global efficiency through the flight

CO_2 emissions are directly linked to fuel consumption. Since hybrid cases optimise the engine operation, emissions are lower throughout the flight and, although on the engine map both the purely hybrid case and the HE DEP BLI case behave similarly, the increase in aerodynamic efficiency and propul-

sive efficiency of the later is translated into lower overall greenhouse gases emissions.

In global efficiency, differences between cases can be observed, where the hybrid cases perform more efficiently than the baseline case. This is indeed largely due to the low *BSFC*, but the combination of better aerodynamic efficiency and high propulsive efficiency puts the case with DEP and BLI above the pure hybrid case.

The results of both studies are shown in Table 4, where fuel savings are expressed as a function of the baseline case as in Equation 8, being m_{fuel} the mass of fuel needed to complete the mission.

$$\text{Fuel savings} = \frac{m_{\text{fuel,baseline}} - m_{\text{fuel}}}{m_{\text{fuel,baseline}}} \tag{8}$$

Table 4: Comparison of results between cases

Case	**Fuel mass** [kg]	**CO_2 emissions** [kg]	**Fuel saved** [%]
Baseline	10.00	30.53	0
Hybrid no DEP	8.82	26.91	11.8
Hybrid with DEP and BLI	8.42	25.72	15.8

Given the results, the most fuel-saving configuration for the same range is the one that benefits from the improved aerodynamic efficiency produced

by the BLI, and has propellers distributed in such a way that they operate with an optimal load with increased propulsive efficiency. This results in the hybrid case with DEP and BLI with a total distribution of 13 engines along the wing, with 40 mm of propeller radius, whose positions are over 31.5 % of the trailing edge and have a draft angle of 1.5°.

It is worth mentioning that, as the objective of the optimisation was to minimise the fuel consumption, pollutant emissions such as NOx, CO or unburnt hydrocarbons have not been studied. Some technologies may be used to mitigate them, such as the use of 3-way catalysts or lean-burn combustion strategies. Not taking into account these pollutant emissions may be especially concerning under new regulations. Further research will be needed to address the problem from that point of view.

5. Conclusions

A hybrid configuration in series that allows the electrical distribution of the different engines on the trailing edge so that the propellers ingest the boundary layer formed in the wing is possible and feasible in RPAS. This allows to reduce their fuel consumption and, therefore, reduce greenhouse gas emissions, maintaining the same maximum range of a conventional aircraft

powered by an ICE. The suction of the flow around the wing by the propellers due to the DEP and BLI configuration increases the aerodynamic efficiency and, by carefully selecting their position, size and distribution on the trailing edge, the propulsive efficiency can be also increased above what is achievable without BLI.

For a low speed, fixed-wing aircraft with an $MTOM$ of 25 kg with optimal DEP and BLI, fuel savings greater than 15 % against a baseline configuration can be achieved for a long-range mission. When compared to a hybrid-electric approach with neither DEP nor BLI, fuel savings of around 5 % can be expected. The decrease in the required fuel mass can be translated directly into a higher payload, a greater mission range, operating costs reductions or a combination of the three.

The results obtained in this manuscript are produced taking into account the extra operating empty mass of the aircraft after adding the components needed for the series hybridisation, as well as the power electronics, wiring and extra motors needed in the DEP plus BLI configuration. Although the extra mass has been estimated by choosing several commercial off-the-shelf components and by comparing with results found in the literature, this estimation is expected to be conservative. By distributing the mass of the

propulsive system over the wing, a reduction in the bending moment in the wing root is achieved, thus enabling a reduction in its structural mass. Taking into account this effect, further increases in the efficiency of a DEP plus BLI configuration are expected.

Declaration of Competing Interest

None declared.

Acknowledgements

The authors wish to thank P. Raga for his help with the setup of the computational simulations.

This research was partially funded by the Agencia Estatal de Investigación of Spain through grant number PID2020-119468RA-I00 / AEI / 10.13039/501100011033. It was also partially funded by the Conselleria d'Innovació, Universitats, Ciència i Societat Digital of the Generalitat Valenciana through grant with expedient number GV/2021/069 of the program for "Grupos de Investigación Emergentes GV/2021".

Nomenclature

Abbreviations

BLI	Boundary layer ingestion
BEMT	Blade Element Model Theory
BSFC	Brake-specific fuel consumption
CFD	Computational fluid dynamics
DEP	Distributed electrical propulsion
ESC	Electronic speed controller
HE	Hybrid electric
ICE	Internal combustion engine
LSB	Laminar separation bubble
RANS	Reynols-averaged Navier-Stokes
RPAS	Remotely piloted aircraft system
TE	Trailing edge
UAV	Unmanned aerial vehicle

Roman letters

$Æ R$	Aspect ratio
b	Wingspan
BS	Base size
c	Chord
C_L	Lift coefficient
C_D	Drag coefficient
C_p	Pressure coefficient
C_f	Friction coefficient
C	Constant
D	Drag
d	Diameter
g	Gravity acceleration
J	Advance ratio
m	Mass
n	Rotational speed
p	Order of convergence
P	Power

R	Range
Re	Reynolds
S	Wing surface
T	Thrust
U	Speed
X	Position across the chord

Greek letters and other symbols

α	Angle of attack
β	Specific range
η_p	Propulsion efficiency
η_e	Electrical efficiency
η_m	Gearbox efficiency
λ	Flight velocity law slope
μ	Viscosity
ρ	Density
τ	Engine torque

References

[1] Single European Sky ATM Research, European Drones Outlook Study, last accessed: 2021-03-10 (2016).
URL http://www.sesarju.eu/sites/default/files/documents/reports/European_Drones_Outlook_Study_2016.pdf

[2] C. L. Nickol, W. J. Haller, Assessment of the performance potential of advanced subsonic transport concepts for NASA's environmentally responsible aviation project, in: 54th AIAA Aerospace Sciences Meeting, San Diego, CA, USA, 2016, pp. 1–21. doi:10.2514/6.2016-1030.

[3] H. Zhang, B. Song, F. Li, J. Xuan, Multidisciplinary design optimization of an electric propulsion system of a hybrid UAV considering wind disturbance rejection capability in the quadrotor mode, Aerospace Science and Technology 110 (2021) 20. doi:10.1016/j.ast.2020.106372.

[4] M. Rostami, A. hamzeh Farajollahi, Aerodynamic performance of mutual interaction tandem propellers with ducted UAV, Aerospace Science and Technology 108 (2021) 10. doi:10.1016/j.ast.2020.106399.

[5] K. E. McKinney, Evaluation of Hybrid-Electric Power System Integration Challenges for Multi-rotor UAS, B.Sc. thesis, Oklahoma State University, Stilwater, OK, USA (2018).

[6] W. J. Fredericks, M. D. Moore, R. C. Busan, Benefits of hybrid-electric propulsion to achieve 4x increase in cruise efficiency for a VTOL aircraft, 2013 International Powered Lift Conference (2013) 1–21doi:10.2514/6.2013-4324.

[7] F. Payri, J. Desantes, Motores de Combustión Interna Alternativos, Editorial Reverté and Editorial UPV, 2011.

[8] J. Heywood, Internal Combustion Engine Fundamentals, McGraw-Hill Education, 1988.

[9] J. Benajes, R. Novella, J. Gómez-Soriano, I. . Barbery, C. Libert, F. Rampanarivo, M. Dabiri, Computational assessment towards understanding the energy conversion and combustion process of lean mixtures in passive pre-chamber ignited engines, Applied Thermal Engineering 178 (2020). doi:10.1016/j.applthermaleng.2020.115501.

[10] T. Nagasawa, Y. Okura, R. Yamada, S. Sato, H. Kosaka, T. Yokomori, N. Iida, Thermal efficiency improvement of super-lean burn spark ig-

nition engine by stratified water insulation on piston top surface, International Journal of Engine Research 22 (2021) 1421–1439. doi:10.1177/1468087420908164.

[11] H. D. Kim, A. T. Perry, P. J. Ansell, A Review of Distributed Electric Propulsion Concepts for Air Vehicle Technology, 2018 AIAA/IEEE Electric Aircraft Technologies Symposium, EATS 2018 (2018). doi:10.2514/6.2018-4998.

[12] J. K. Ausserer, F. G. Harmon, Integration, validation, and testing of a hybrid-electric propulsion system for a small remotely-piloted aircraft, in: 10th Annual International Energy Conversion Engineering Conference, Atlanta, GA, USA, 2012, pp. 1–11. doi:10.2514/6.2012-4239.

[13] F. G. Harmon, A. A. Frank, J. J. Chattot, Conceptual design and simulation of a small hybrid-electric unmanned aerial vehicle, Journal of Aircraft 43 (5) (2006) 1490–1498. doi:10.2514/1.15816.

[14] C. Kim, E. Namgoong, S. Lee, T. Kim, H. Kim, Fuel economy optimization for parallel hybrid vehicles with CVT, Technical Paper 1999-01-1148, SAE (1999). doi:10.4271/1999-01-1148.

[15] I. H. Mengistu, A small internal combustion engine testing for a hybrid-

electric remotely-piloted aircraft, Master's thesis, Air Force Institute of Technology, Wright-Patterson Air Force Base, OH, USA (2011).

[16] J. Lieh, E. Spahr, A. Behbahani, J. Hoying, Design of hybrid propulsion systems for unmanned aerial vehicles, in: 47th AIAA/ASME/SAE/ASEE Joint Propulsion Conference and Exhibit, San Diego, CA, USA, 2011, pp. 1–14. doi:10.2514/6.2011-6146.

[17] A. M. Stoll, J. Bevirt, M. D. Moore, W. J. Fredericks, N. K. Borer, Drag Reduction Through Distributed Electric Propulsion, in: 15th AIAA Aviation Technology, Integration, and Operations Conference, Atlanta, GA, USA, 2015, pp. 22–26. doi:10.2514/6.2015-3188.

[18] A. M. Stoll, Comparison of CFD and experimental results of the leap tech distributed electric propulsion blown wing, in: 15th AIAA Aviation Technology, Integration, and Operations Conference, Dallas, TX, USA, 2015, pp. 22–26. doi:10.2514/6.2015-3188.

[19] C. Xue, Z. Zhou, Propeller-wing coupled aerodynamic design based on desired propeller slipstream, Aerospace Science and Technology 97 (2020) 16. doi:10.1016/j.ast.2019.105556.

[20] C. Xue, Z. Zhou, Inverse aerodynamic design for DEP propeller based

on desired propeller slipstream, Aerospace Science and Technology 102 (2020) 9. doi:10.1016/j.ast.2020.105820.

[21] P. Lv, D. Ragni, T. Hartuc, L. Veldhuis, A. G. Rao, Experimental investigation of the flow mechanisms associated with a wake-ingesting propulsor, AIAA Journal 55 (4) (2017) 1332–1342. doi:10.2514/1.J055292.

[22] L. Leifsson, A. Ko, W. H. Mason, J. A. Schetz, B. Grossman, R. T. Haftka, Multidisciplinary design optimization of blended-wing-body transport aircraft with distributed propulsion, Aerospace Science and Technology 25 (1) (2013) 16–28. doi:10.1016/j.ast.2011.12.004.

[23] J. L. Felder, H. D. Kim, G. V. Brown, Turboelectric distributed propulsion engine cycle analysis for hybrid-wing-body aircraft, 47th AIAA Aerospace Sciences Meeting including the New Horizons Forum and Aerospace Exposition (2009) 1–25doi:10.2514/6.2009-1132.

[24] J. A. Schetz, S. Hosder, V. Dippold, J. Walker, Propulsion and aerodynamic performance evaluation of jet-wing distributed propulsion, Aerospace Science and Technology 14 (1) (2010) 1–10. doi:10.1016/j.ast.2009.06.010.

[25] D. K. Hall, A. C. Huang, A. Uranga, E. M. Greitzer, M. Drela,

S. Sato, Boundary layer ingestion propulsion benefit for transport aircraft, Journal of Propulsion and Power 33 (5) (2017) 1118–1129. doi:10.2514/1.B36321.

[26] L. Teperin, Investigation on Boundary Layer Ingestion Propulsion for UAVs, in: International Micro Air Vehicle Conference and Flight Competition (IMAV), Toulousse, France, 2017, pp. 293–300.

[27] A. Martínez Fernández, H. Smith, Effect of a fuselage boundary layer ingesting propulsor on airframe forces and moments, Aerospace Science and Technology 100 (2020) 105808. doi:10.1016/j.ast.2020.105808.

[28] S. Samuelsson, T. Grönstedt, Performance analysis of turbo-electric propulsion system with fuselage boundary layer ingestion, Aerospace Science and Technology 109 (2021) 10. doi:10.1016/j.ast.2020.106412.

[29] C. Goldberg, D. Nalianda, D. MacManus, P. Pilidis, J. Felder, Installed performance assessment of a boundary layer ingesting distributed propulsion system at design point, 52nd AIAA/SAE/ASEE Joint Propulsion Conference, 2016 52 (1) (2016) 1–22. doi:10.2514/6.2016-4800.

[30] España, Real Decreto 1036/2017, Boletín Oficial del Estado, BOE-A-2017-15721 (2017).
URL https://www.boe.es/eli/es/rd/2017/12/15/1036

[31] UAV Factory USA LLC., Penguin C UAS, last accessed: 2021-03-10.
URL https://www.uavfactory.com

[32] F. D. David Willermark, GT-power simulation report, last accessed: 2021-03-10 (2009).
URL http://www.chalmersverateam.se/Rapporter/GTPowerGX35.pdf

[33] J. Schoemann, M. Hornung, Modeling of hybrid-electric propulsion systems for small unmanned aerial vehicles, in: 12th AIAA Aviation Technology, Integration and Operations (ATIO) Conference and 14th AIAA/ISSMO Multidisciplinary Analysis and Optimization Conference, Indianapolis, IN, USA, 2012, pp. 1–18. doi:10.2514/6.2012-5610.

[34] C. A. Lyon, A. P. Broeren, P. Giguere, A. Gopalarathnam, M. S. Selig, Summary of Low-Speed Airfoil Data - Volume 3, Vol. 3, SoarTech Publications, Virginia Beach, VA, USA, 1997.

[35] Selig, Donovan, Fraser, Airfoils at Low Speeds, H.A. Stokey, Virginia Beach, VA, USA, 1989.

[36] M. S. Selig, Low Reynolds Number Airfoil Design Lecture Notes - Various Approaches to Airfoil Design, last accessed: 2021-09-27 (2003). URL https://m-selig.ae.illinois.edu/pubs/Selig-2003-VKI-LRN-Airfoil-Design-Lecture-Series.pdf

[37] D. M. Sutton, Experimental Characterization of the Effects of Freestream Turbulence Intensity on the SD7003 Airfoil at Low Reynolds Numbers, Ph.D. thesis, University of Toronto, Toronto, ON, Canada (2015).

[38] S. Hoerner, Fluid-Dynamic Drag, Hoerner Fluid Dynamics, 1965.

[39] M. Niţă, D. Scholz, Estimating the oswald factor from basic aircraft geometrical parameters, in: Deutscher Luft- und Raumfahrtkongress, Hamburg University Of Applied Sciences: Hamburg, Germany, 2012.

[40] R. W. Deters, G. K. Ananda, M. S. Selig, Reynolds number effects on the performance of small-scale propellers, in: 32nd AIAA Applied Aerodynamics Conference, 2014, pp. 1–43. doi:10.2514/6.2014-2151.

[41] S. Schmidt, M. Breuer, Hybrid LES-URANS methodology for the prediction of non-equilibrium wall-bounded internal and external flows, Computers and Fluids 96 (2014) 226–252. doi:10.1016/j.compfluid.2014.03.020.

[42] L. H. Smith, Wake ingestion propulsion benefit, Journal of Propulsion and Power 9 (1) (1993) 74–82. doi:10.2514/3.11487.

[43] A. Torregrosa, A. Gil, P. Quintero, A. Ammirati, H. Denayer, W. Desmet, Prediction of flow induced vibration of a flat plate located after a bluff wall mounted obstacle, Journal of Wind Engineering and Industrial Aerodynamics 190 (January) (2019) 23–39. doi:10.1016/j.jweia.2019.04.008.
URL https://doi.org/10.1016/j.jweia.2019.04.008

[44] B. T. Blumenthal, A. A. Elmiligui, K. A. Geiselhart, R. L. Campbell, M. D. Maughmer, S. Schmitz, Computational investigation of a boundary-layer-ingestion propulsion system, Journal of Aircraft 55 (3) (2018) 1141–1153. doi:10.2514/1.C034454.

[45] M. Cerny, C. Breitsamter, Investigation of small-scale propellers un-

der non-axial inflow conditions, Aerospace Science and Technology 106 (2020) 14. doi:10.1016/j.ast.2020.106048.

[46] P. L. Roe, Approximate Riemann Solvers, Parameter Vectors, and Difference Schemes, Journal of Computational Physics 43 (1981) 357–372.

[47] V. Venkatakrishnan, On the accuracy of limiters and convergence to steady state solutions, AIAA 93-0880 (1993). doi:10.2514/6.1993-880.

[48] W. L. Oberkampf, T. G. Trucano, Verification and validation in computational fluid dynamics, Progress in Aerospace Sciences 38 (2002) 209–272. doi:10.1201/b19031-50.

[49] P. J. Roache, Perspective: A Method for Uniform Reporting of Grid Refinement Studies (1994).

[50] O. Gur, A. Rosen, Comparison between blade-element models of propellers, Aeronautical Journal 112 (1138) (2008) 689–704. doi:10.1017/S0001924000002669.

[51] XFLR5, last accessed: 2021-03-10.
URL http://www.xflr5.tech/xflr5.htm

[52] M. Drela, XFOIL Subsonic Airfoil Development System, last accessed: 2021-03-10.

URL https://web.mit.edu/drela/Public/web/xfoil/

[53] W. Zhao, A Broyden–Fletcher–Goldfarb–Shanno algorithm for reliability-based design optimization, Applied Mathematical Modelling 92 (2021) 447–465. doi:10.1016/j.apm.2020.11.012.

[54] APC, APC Propeller RPM Limits, APC website 95776 (530) (2016) 95776.

[55] Serrano, J.R. and Tiseira, A.O. and García-Cuevas, L.M. and Varela, P., Computational study of the propeller position effects in wing-mounted, distributed electric propulsion with boundary layer ingestion in a 25 kg remotely piloted aircraft, Drones 5 (3) (2021). doi:10.3390/drones5030056.